A NOVEL IMAGE PROCESSING ALGORITHM FOR ENHANCING THE PROBABILITY OF DETECTION OF FLAWS IN X-RAY IMAGES

Nawapak Eua-Anant, Ibrahim Elshafiey*, Lalita Udpa*,
and Joseph Nahum Gray*
Department of Electrical Engineering
and Computer Engineering
Iowa State University
Ames, IA 50011

*Center for Nondestructive Evaluation
Iowa State University
Ames, IA 50011

INTRODUCTION

Application of Digital Signal Processing (DSP) techniques in x-ray radiography is a field that is gaining a rapidly growing interest. Dealing with digital x-ray images and enhancing these images using DSP techniques allow the automation of x-ray inspection, which offers several advantages over the traditional film-based inspection. These advantages include reducing the inspection time and cost requirements, obtaing a consistent decision regarding the integrity of the object under test, and allowing the use of real-time inspection [1]. Typically processing of x-ray images to detect and size flaws involves edge detection. In this paper, we primarily focus on an image processing algorithm that is based on a new Gaussian weighted image moment vector edge operator. Application of this operator enhances image edges and suppresses the noise, which results in a significant improvement in the probability of detection of flaws in x-ray images.

EDGE DETECTION

Edges are defined wherever there are abrupt changes in the image attributes, such as intensity, texture and color. Edge detection techniques are employed to detect such changes. Edge operators can be classified as gradient-based [2, 3, 4], Laplacian-based [5], moment-based [6, 7, 8, 9] or surface fitting edge operators [10]. Conceptually, the gradient and moment-based edge operators estimate the gradient of an image by convolving the image with a set of directional difference masks. X-ray image analysis often requires edge detection at different scales. The conventional edge operators, using fixed size directional difference masks, do not posses the multiscale feature required for handling multiscale edge detection problems. Multiscale edge operators detect edges at various scales and have better noise suppression ability by virtue of the larger, smoother and size-adjustable difference mask [3, 4, 5, 7, 9]. However, there is a trade off between the accuracy of edge localization and noise suppression. In this paper, a new multiscale edge operator is developed using the concept of mechanical moment and a vector model for an image.

Review of Progress in Quantitative Nondestructive Evaluation, Vol. 15
Edited by D.O. Thompson and D.E. Chimenti, Plenum Press, New York, 1996

THE IMAGE MOMENT VECTOR OPERATOR

In mechanics, the moment of an object about a point or axis is generally a measure of its tendency to turn or rotate the object about the point or axis. The approach of using the concept of mechanical moment for edge detection in image processing was inspired by the capability of moment to detect inhomogeneity in an object. The centroid of a homogeneous object coincides with the center of gravity of the object. For an inhomogeneous object with no more than one axis of symmetry, the centroid and the center of gravity are normally different. Consequently, the presence of moment at the centroid due to weight of the object indicates the inhomogeneity of an object.

To allow the use of mechanical moment formula, a vector model of an image was proposed [9]. A vector model of an image is defined as an array of intensity vectors, denoted by

$$\vec{P}(x,y) = P(x,y) \cdot \vec{n}, \tag{1}$$

where $\vec{n}$ is the normal vector of the image plane and $P(x,y)$ is the light intensity of pixel (x,y). Applying the moment formula to an image, an image moment vector $\vec{M}(i,j)$ of a neighborhood N with respect to the observation point (i,j) is given by

$$\vec{M}(i,j) = \sum_{\substack{(x,y)\in N \\ (x,y)\neq(i,j)}} \vec{r}(x,y) \times \vec{P}(x,y), \tag{2}$$

where $\vec{r}(x,y)$ is the position vector from point (i,j) to point (x,y) and N is a predefined circular neighborhood area centered at point (i,j). The array of image moment vectors is used to form the image moment vector map. From the vector cross products in Equation (2), the Image Moment Vector (IMV) operator can be divided into x and y-components, i.e.,

$$M_x(i,j) = \sum_{\substack{(x,y)\in N \\ (x,y)\neq(i,j)}} (y-j) \cdot P(x,y) \tag{3}$$

and

$$M_y(i,j) = \sum_{\substack{(x,y)\in N \\ (x,y)\neq(i,j)}} -(x-i) \cdot P(x,y). \tag{4}$$

Each component is a convolution of the image and the directional difference mask. An example of the directional difference mask in x-direction and its cross section at $y = 0$ are shown in Figure 1. Due to symmetry, the image moment of a homogeneous area vanishes while that of an inhomogeneous area including an edge is nonzero. Degradation noise assumed to be directionally homogeneous does not affect the image moment. Consequently, the edge detection scheme using the IMV is very robust. However, in contrast to visual systems, the IMV difference mask coefficients are such that pixels farther away from the observation point are weighted higher than pixels closer to the observation point. This leads to problems in edge localization and the next section describes a modified form of the IMV.

THE GAUSSIAN WEIGHTED IMAGE MOMENT VECTOR OPERATOR

To improve edge localization performance, the difference mask coefficients of the operator must be properly rearranged in form so that the coefficients closer to the center of the mask are larger and then smoothly decreased with the distance from the center of the mask. In this paper, we modified the IMV by first, dividing the cross product term in Equation 2 by the magnitude of the position vector in order to equalize the effect of the position vector and then multiplying the cross product term by a smooth and monotonically

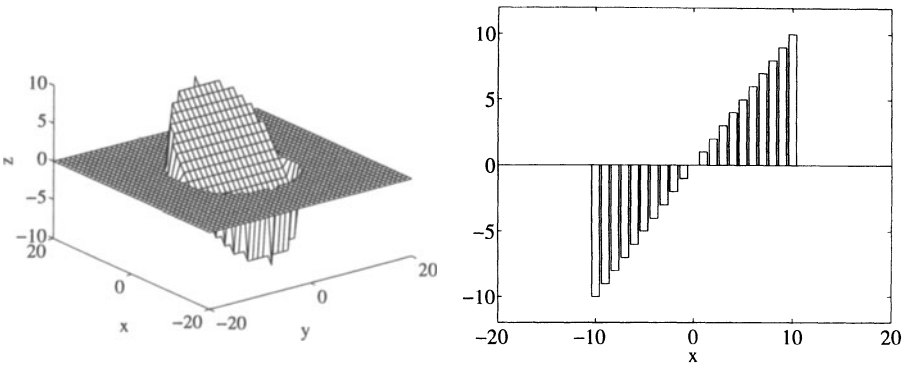

(a) (b)

Figure 1: (a) The directional difference mask in x-direction of the IMV and (b) The cross section of the difference mask at $y = 0$

decreasing function of the distance. Using the popular Gaussian function as a weighting function, the Gaussian Weighted Image Moment Vector (GWIMV) operator is given by

$$\vec{M}(i,j) = \sum_{(x,y)\neq(i,j)} G(r(x,y)) \cdot \frac{\vec{r}(x,y) \times \vec{P}(x,y)}{r(x,y)}, \tag{5}$$

where $r(x,y)$ is the magnitude of $\vec{r}(x,y)$ and $G(r)$ is the Gaussian function ;

$$G(r) = \exp\left(-\frac{r^2}{2\sigma^2}\right). \tag{6}$$

The parameter σ of the Gaussian function controls the shape of difference masks. The performance of the GWIMV, therefore, directly depends the parameter σ. The GWIMV can be separated in to two convolutions;

$$M_x(i,j) = \sum_{(x,y)\neq(i,j)} \frac{(y-j)}{r(x,y)} \cdot \exp\left(-\frac{(r(x,y))^2}{2\sigma^2}\right) \cdot P(x,y) \tag{7}$$

$$= -G_y * P(x,y) \approx \frac{\partial P(x,y)}{\partial y} \tag{8}$$

and

$$M_y(i,j) = \sum_{(x,y)\neq(i,j)} \frac{-(x-i)}{r(x,y)} \cdot \exp\left(-\frac{(r(x,y))^2}{2\sigma^2}\right) \cdot P(x,y) \tag{9}$$

$$= G_x * P(x,y) \approx \frac{-\partial P(x,y)}{\partial x}, \tag{10}$$

where G_x and G_y are difference masks of the GWIMV in x and y directions respectively. The example of the difference mask in x-direction of the GWIMV and its cross section at $y = 0$ are illustrated in Figure 2. The results from Equations (8) and (10) form the Hamiltonian gradient vector field of an image in contrast to the gradient vector field which results from the gradient-based edge operators. Examples of the vector map and the normalized magnitude map of image moment vectors, namely an edge image, are displayed in Figure 3. For the GWIMV, if σ is small, i.e., difference masks are steep, the GWIMV will result in good edge localization but poor noise suppression. The effects of σ on edge images are illustrated in Figure 4. Large values of σ result in thicker edges indicating poor edge localization as shown in Figure 4-b to 4-e while they give rise to good noise suppression as shown in Figure 4-g to 4-j. At this point, the trade off between edge localization and noise suppression brings to the problem of selecting the optimum value for σ.

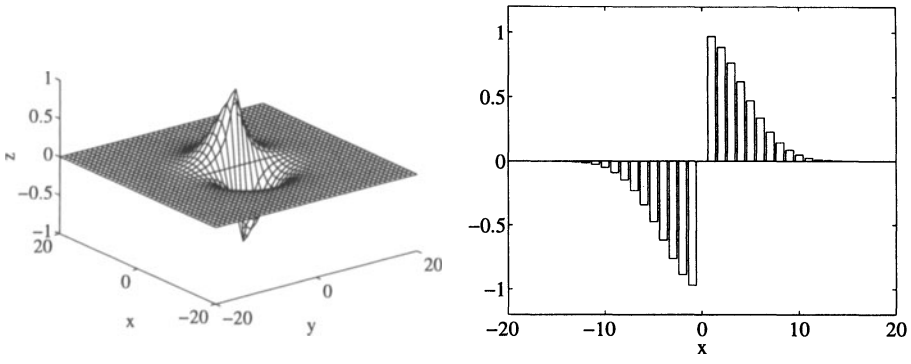

(a) (b)

Figure 2: (a) The directional difference mask in x-direction of the GWIMV and (b) The cross section of the difference mask at $y = 0$

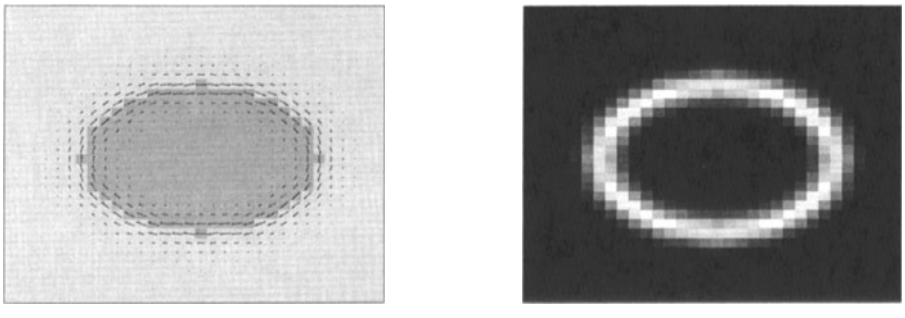

(a) (b)

Figure 3: (a) The image moment vector map with $\sigma = 1.4$ and (b) The normalized magnitude map of the image moment vectors or the edge image

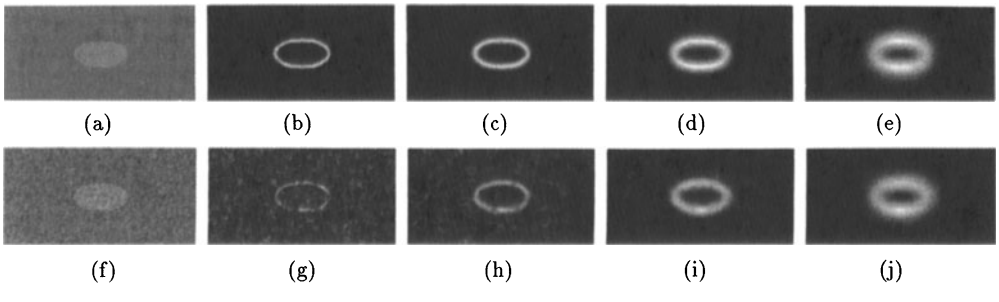

(a) (b) (c) (d) (e)

(f) (g) (h) (i) (j)

Figure 4: (a) The original image without noise and edge images with (b) $\sigma = 1$, (c) $\sigma = 2$, (d) $\sigma = 4.2$, (e) $\sigma = 8$. (f) The noisy image degraded by the additive Gaussian noise with SNR = 2, and edge images with (g) $\sigma = 1$, (h) $\sigma = 2$, (i) $\sigma = 4.2$, (j) $\sigma = 8$

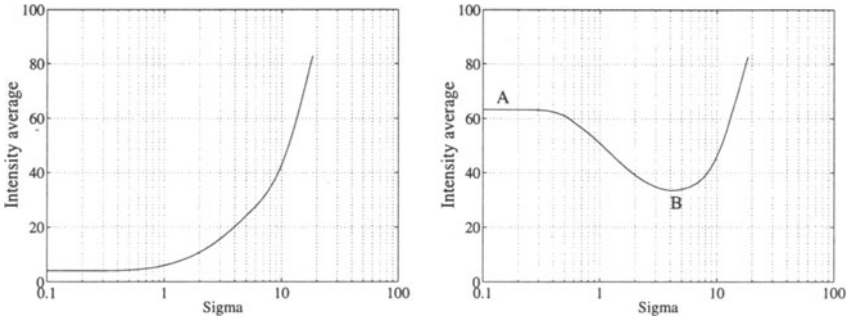

(a) (b)

Figure 5: (a) The intensity average and σ curve of the image in Figure 4-a. (b) The intensity average and σ curve of the image in Figure 4-f.

SELECTION OF σ FOR MULTISCALE PROBLEMS

The choice of the value of σ, for an edge operator, determines the size scale of the features that can be represented by the extracted edges. Small values of σ is suitable for extracting edges of small features, while large values of σ can be used to extract large scale edges. According to scale-space theorem, σ is a meaningful measure of scale [4, 11]. For a noise corrupted image, small values of σ results in a large number of bright pixels due to the noise, and also large values of σ produces large number of bright pixels, due to the increase in the extracted edge size. The "best" edge image should have the least number of bright pixels that are generated from noise, and also the sharpest possible edge. This image corresponds should thus have the smallest number of bright pixels, which sets The minimum intensity average criterion as the basis for selecting the optimum value of σ.

In a multiscale problem, a plot of the intensity average of a normalized edge image vs. the parameter σ contains multiscale information about behavior of edges. The number of local minima in the intensity average curve indicates the number of scales that exist. The existence of local minima at some scales in the intensity average curve guarantees the existence of objects at that scale. Examples of the intensity average curves of images in Figures 4-a and 4-f are shown in Figure 5. The x-axis of Figure 5 is displayed in logarithmic scale in accordance with scales in nature which usually exhibits exponential scales. For a "clear" image, as shown in Figure 4-a, there is only one minimum point in the intensity average curve as shown in Figure 5-a. This point represents the scale of the ellipsoid in Figure 4-a. On the other hand, for a noisy image in Figure 4-f, there are two local minima, as expected, at points A and B in the curve in Figure 5-b. The first is the smallest σ value representing the scale of noise. The second is at $\sigma = 4.2$ representing the scale of the ellipsoid. Among the images shown in Figure 4, the best edge images, in the sense of minimum intensity average criterion, are Figures 4-b and 4-i. The minimum intensity average criterion, thus, offers an automatic method for selecting the optimum σ.

FLAW ENHANCEMENT PROCESS

In this paper, the first step in flaw detection is to obtain a flaw image by subtracting a reference image from the x-ray image. A model generated reference image is used here in the subtraction process. In dealing with experimental radiographs, the reference image should be registered with respect to the real image, and this is done using local or global registration techniques as explained in [12]. After subtraction, the edge enhancement process is then performed by convolving the flaw image with a pair of GWIMV directional

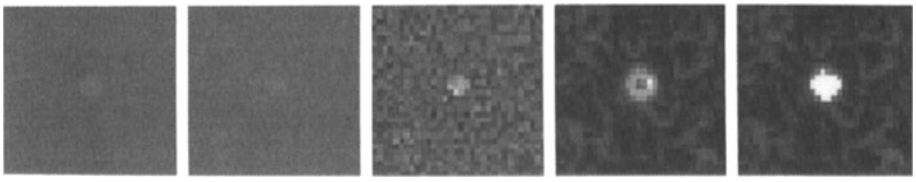

(a) (b) (c) (d) (e)

Figure 6: (a) The original flaw image. (b) The noisy flaw image. (c) The histogram stretching image of Figure b. (d) The optimum edge image. (e) The enhanced flaw image.

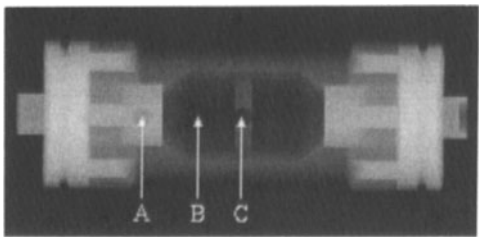

Figure 7: The simulated x-ray image of the object with spherical flaws with diameter varied from 1 to 5 mm. in 3 locations.

difference masks with the optimum σ selected based on the minimum intensity average criterion. Once a suitable edge image is obtained, a filling process then fills up all pixels surrounded by edges with the nearest local maximum pixel value. Hence the enhanced flaw in the image is usually larger than the original flaw itself because edge pixels are included in the enhanced flaw. An example of the enhanced flaw image compared to the original flaw image is shown in Figure 6.

RESULTS

The probability of detection calculation

In order to evaluate the flaw enhancement process, the probability of detection of the flaw (POD) in the enhanced flaw image is compared with the POD of the original flaw image. The POD calculation, in this paper, is based on the Bayes classification. By considering the histograms of flaw pixels and background pixels, a threshold value satisfying the Bayes optimal decision rule is selected which results in the minimum classification error. In the original flaw image, due to the large number of background pixels relative to the number of flaw pixels, the background pixel histogram usually obscures the peak of the flaw pixel histogram. Therefore, the POD calculation is limited to a predefined window around the flaw. The POD of the original flaw image is calculated as the number of correctly classified flaw pixels divided by the number of total flaw pixels. Using the same decision rule, the POD of the enhanced flaw image is calculated as the number of correctly classified flaw and edge pixels divided by the number of total flaw and edge pixels. For both original and enhanced flaw images, the probability of error (POE) is defined as the number of misclassified pixels divided by the number of total pixels in the area of consideration.

Experimental Results

Simulated x-ray images of size 256 × 128 pixels of an object with spherical flaws embedded in three locations, shown in Figure 7, were used in this experiment. The flaw diameters varied from 1 to 5 mm. Histograms of 10 x-ray images with the same flaw size

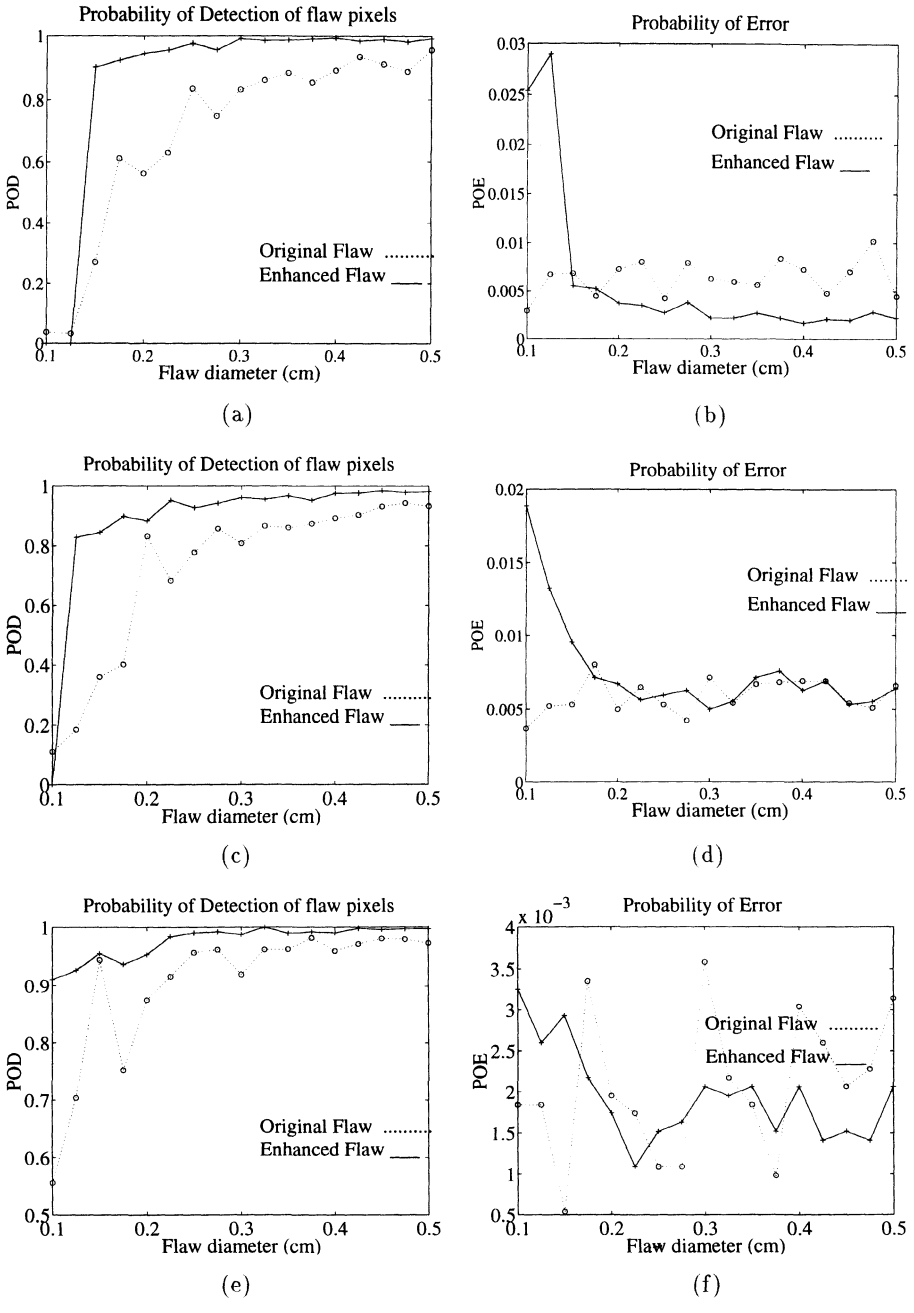

Figure 8: The probability of detection of flaws and the probability of error. (a) and (b) flaws at location A shown in Figure 7. (c) and (d) flaws at location B shown in Figure 7. (e) and (f) flaws at location C shown in Figure 7.

and different noise sequences were used to calculate each of the POD and the POE values. The POD and POE curves of flaws at location A, B and C are displayed in Figure 8. As shown, when the flaw size is very small, the POD of both original and enhanced flaw images is very low and the POE of enhanced flaw images is relatively higher than that of the original flaw images. This is due to the fact that the apparent size of a flaw is very small relative to the size of the area of consideration and also that the flaw contrast is very low. As flaw size increases, the POD of the enhanced flaw image increases significantly faster than that of the original flaw image, while the POE reduces rapidly. The POD and POE of both original and enhanced flaw images tend to converge to 1 and 0 respectively with the increase of flaw size, and the results of the enhanced flaw image are still superior to those of the original flaw image.

CONCLUSIONS

A new technique for detecting and enhancing flaws in x-ray images is presented. The method depends on a Gaussian weighted image moment vector operator for extracting object edges at various scales. The scaling parameter σ of the Gaussian weighted image moment vector operator is automatically selected based on the minimum intensity average criterion to ensure detection of object edges. Resultant edge images indicate that the method is very robust and sensitive even for a low contrast flaw embedded in noisy x-ray images. Preliminary results using simulated x-ray images have shown that this technique significantly improves the probability of detection of flaw and also reduces the probability of error.

REFERENCES

1 R. M. Wallingford and J. N. Gray, "Application of Real-Time Image Processing and Calibration Techniques to Real-Time X-ray NDE," *Review of Progress in QNDE*, vol. 13, pp. 755-762, 1994.

2 A. Rosenfield and M. Thurston, "Edge and Curve Detection for Visual Scene Analysis," *IEEE Trans. Comput.*, vol. C-20, no. 5, pp. 562-569, 1971.

3 J. F. Canny, "A Computational Approach to Edge Detection," *IEEE Trans. Pattern Anal. Machine Intell.*, vol. PAMI-8, no. 6, pp. 679-698, Nov. 1986.

4 B. M. ter Haar Romeny *et al.*, "Higher Order Differential Structure of Images," *Image and Vision Computing*, vol. 12, no. 6, pp. 317-388, July/Aug 1994.

5 D. C. Marr and E. Hildreth, "Theory of Edge Detection," *Proc. Roy. Soc. London*, Vol. B 204, pp. 301-328, 1979.

6 R. Machuca and A. L. Gilbert, "Finding Edges in Noisy Scenes," *IEEE Trans. Pattern Anal. Machine Intell.*, vol. PAMI-3, no. 1, pp. 103-111, Jan. 1981.

7 A. P. Reeves *et al.*, "A Moment-Based Two-dimensional Edge Operator," *Proc. IEEE Comput. Vision Pattern Recognition*, pp.312-317, 1983.

8 L. M. Luo *et al.*, "A Moment-Based Three-Dimensional Edge Operator," *IEEE Trans. Biomedical Engineering*, vol. 40, no. 7, pp. 693-703, July 1993.

9 N. Eua-Anant and L. Udpa, "Edge Detection Using Image Moment vector," *Proceedings of the 4th annual Midwest Electro-Technology conference*, Iowa State University, pp 23-26, 1995.

10 V. S. Nalwa and T. O. Binford, "On Detecting Edges," *IEEE Trans. Pattern Anal. Machine Intell.*, vol. PAMI-8, no. 6, Nov. 1986.

11 L. M. J. Florak *et al.*, "Scale and the Differential Structure of an Image," *Image and Vision computing* , vol. 10, no. 6, pp. 376-388, July/August 1992.

12 J. A. Khan, Analysis and Interpretation of Scanning Acoustic Microscopy Images, Master thesis, Iowa State University, 1994.